

# Coastal Imagery Analysis and Breaking Wave Type Estimation with Machine Learning

Jorge Arce-Garro<sup>\*1</sup>, Taewon Cho<sup>\*2</sup>, Hye Rin Lindsay Lee<sup>\*3</sup>,  
Ryleigh Moore<sup>\*4</sup>, Risa R. Sayre<sup>\*5</sup>, Yao Xuan<sup>\*6</sup>, Zitong Zhou<sup>\*7</sup>

Faculty Mentors: Matthew Farthing<sup>8</sup>, Tyler Hesser<sup>8</sup>, Harry Lee<sup>9</sup>

## Abstract

Classifying and identifying ocean wave breaker types is important to guarantee the safety and success of both civilian and military operations occurring in and around the surfzone. Current high fidelity numerical models are sensitive to boundary conditions and are not fast enough to solve this problem in the time frame needed. An empirical parameterization for wave breaking type is employed using offshore wave conditions and surfzone slopes estimated from an inverse method using nearshore video imagery. Machine learning models are attractive due to their speed and ability to predict information using less information than other methods. In this paper, a direct method is used to label training data for multiple machine learning approaches in order to predict the wave breaker types given an image and offshore wave conditions.

## 1 Introduction

Estimating the coastal hydrodynamics and ocean conditions is important for both the safety and success of civil works and military missions of the United States armed forces. Military operations can require the transport of people and equipment from deep water to the beach. However, the dynamics of waves in the narrow strip between these two zones must be better understood in order to avoid navigational difficulties, damage to ships, and even deaths due to treacherous plunging waves. The main cause of this danger is the process of wave breaking, since this is the mechanism by which a wave can release energy on its surroundings [1]. Therefore, wave breaking must be analyzed first in order to provide recommendations or predictions to avoid this damage.

## 2 Objective

This study focuses on developing an algorithm to predict the type of breaking waves at a beach for a given moment in time; this will be done by using the most readily available nearshore wave conditions, imagery, and corresponding data for the wave height and period. Ultimately, this algorithm will be able to employ forecasts of wave height and period data as well as an image of the beach to generate probabilistic forecasts of the breaking types.

---

<sup>\*</sup> Denotes co-first authors listed in alphabetical order by last name.

<sup>1</sup>Department of Mathematics, University of Michigan

<sup>2</sup>Department of Mathematics, Virginia Tech

<sup>3</sup>Department of Mathematics, Applied Mathematics and Statistics, Case Western Reserve University

<sup>4</sup>Department of Mathematics, University of Utah

<sup>5</sup>Department of Environmental Sciences and Engineering, University of North Carolina - Chapel Hill

<sup>6</sup>Department of Mathematics, University of California - Santa Barbara

<sup>7</sup>Department of Energy Resources Engineering, Stanford Universiy

<sup>8</sup>United States Army Corps of Engineers, Engineer Reseach and Development Center (USACE, ERDC)

<sup>9</sup>Department of Civil and Environmental Engineering, University of Hawai'i at Mānoa



Figure 1: Wave Breaker Types at Duck, N.C. - Source: Brodie *et al.* (2018)

Table 1: Criteria for breaking wave classification, where  $I$  is the Iribarren number. - Source: Battjes et al. (1975)

Breaker type	$I$ range
Spilling	$I < 0.5$
Plunging	$0.5 < I < 3.3$
Surging	$I > 3.3$

## 2.1 Wave Breaking

As waves come from deep water to shore, forces from the seabed slow them down and reduce their wavelength. Conservation of energy flux requires their heights to increase, in a phenomenon known as shoaling [2]. The shoaling process causes the top of the wave, the crest, to move faster than the bottom, the trough, which eventually causes the crest to spill over and to break, releasing the potential energy that has built up from the slowing of the wave.

There are three main wave breaking types that are being considered in this research: spilling, plunging, and surging. The breaking types of waves are determined by the wave height, wave period, and the underwater topography near the shore, or the bathymetry. (See Figure 1). In general, the spilling and collapsing waves are considered safe for boats trying to cross the surfzone, the area where breaking waves are observed. On the other hand, plunging waves are the most dangerous for boats. Their steep crests plunge violently when they break, exerting a sudden force that can disrupt a boat's path, or even capsize it.

## 2.2 Classification of Breaking Types

An approach found in the literature to classify breaker types is the Iribarren number [1]. Let  $m$  denote the beach slope, and let  $H_d$  and  $L_d$  denote the height and wavelength of a wave in deep water, respectively. The Iribarren number at deep water is the dimensionless parameter defined by

$$I = \frac{m}{\sqrt{H_d/L_d}}. \quad (1)$$

The criteria in Table 1 have been established for breaking wave classification empirically [3].

The Table 1 and equation (1) are deduced from breaking waves using constant slopes. The actual beach geometries differ significantly from the assumption of constant slopes, especially in the surfzone.

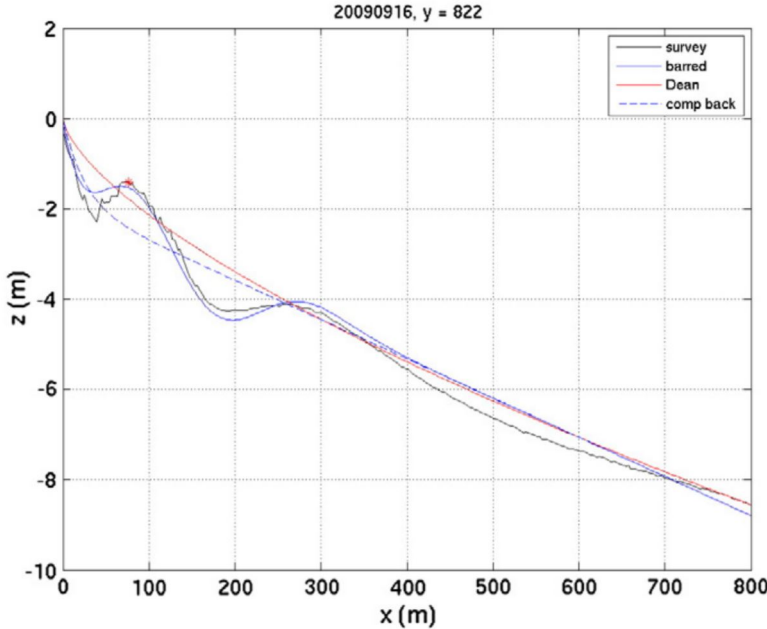


Figure 2: Comparing bathymetry approximations from varying methods [5]

### 2.3 Estimating Bathymetry

Calculation of the Iribarren number requires the bathymetry in order to estimate the slope. A first approximation can be given by an equilibrium beach profile, or Dean profile [4], which consists of a simple convex parametrization of the form  $h = Ay^{2/3}$ , where  $h$  is the water depth, and  $y$  is the offshore distance. The flaw of this model is that it uses an unrealistic topography which does not take into account sand bars - modulations in the sea bed usually caused when storm waves erode the shore and deposit sediment in intermediate (often between 2 and 6 meter) depths. For reference, see Figure 2. The sand bars are crucial components when it comes to classifying breaking types, as they often provide the first line of breaking waves that shape the dimensions of the surfzone.

As an additional complication, bathymetry is dynamic; it is constantly changing due to wave interaction and sediment transport [6]. In order to account for quickly changing bathymetry, the interest in bathymetry estimations from remotely collected data has increased over the years. There are several techniques available that use aerial visual inputs such as video imagery [7], surfzone pictures [5, 8], and Light Detection and Range (LIDAR) measurements [9, 10]. The most easily obtainable source of aerial visual input are overhead pictures of the surfzone, which can be generated by a drone. This study uses the algorithm by Holman *et al.* [8] to use this aerial imagery to identify the 2D coordinates of the shoreline and sand bar into a parametric estimation of the 2D bathymetry.

Once a bathymetry estimate is available, it must be noted that the slope in general is not constant over the seafloor. It can be argued that the slope values near the breaking point, where the wave first breaks, are relevant to the breaking process; therefore, one of these slope values should be picked and used in (1).

## 3 Approach

This report describes two approaches to solve the problem of classifying the breaker type. The first method is a direct approach resulting in an Iribarren number calculation, and the second approach is a machine learning method. This initial approach is able to predict the expected breaking wave types in its own right, and also it will be used to label the training data for the machine learning model with a breaker type. Subsections 3.1 and 3.2 describe these 2 approaches and their differences.



Figure 3: Three types of wave images from an Argus monitoring system at Egmond aan Zee - Source: Flanders Marine Institute

The following data is used for both approaches:

- Imagery data: An Argus monitoring system was used to produced imagery data of the coastline near the USACE Field Research Facility (FRF) in Duck, NC. The Argus monitoring system was developed by Oregon State University's Coastal Imaging Lab, and it uses six different cameras pointing at different direction to produce a 180° view of the coast. This system samples every half an hour to an hour all year round and produces a number of imagery products, but for this project we will focus on two different types of images: time exposure (TIMEX) and variance (VAR) images taken over 10 minute time span with a frequency of 2 Hz from 2015 to 2017 (See Figure 3).
- Offshore wave height ( $H$ ) and period ( $T$ ) data: The wave heights and periods coming to shore vary at any given moment in time. The expected values, or averages, of these 2 physical quantities are collected by an acoustic wave and current meter (AWAC) from sensors approximately 1 km offshore of Duck, NC. The significant wave height ( $H_s$ ) is used as a proxy for offshore wave height, and the period is approximated by the sea surface wave period at variance spectral density maximum ( $T_p$ ). It is assumed that these averages remain spatially constant along the entire beach. This is a reasonable assumption, as the coastline region under this study is relatively small at only 2 km in length.

In order to gather offshore information, the AWAC takes samples over approximately 22 minute intervals. Specifically, the significant wave height

$$H_s = 4\sqrt{m_o}$$

is determined from the zeroth moment

$$m_0 = \int_0^\infty E(f) df$$

of the energy function, where  $f$  is the frequency, and  $E$  is the energy. The zeroth moment is the total area under the wave energy density spectrum [11]. For the wave length, the value

$$T_p = \frac{1}{f_o},$$

where  $f_o$  is the frequency associated with the highest amplitude of the wave energy spectrum [11].

Finally, the offshore wave length  $L$  is calculated using the dispersion relationship

$$\sigma^2 = g\kappa \tanh(\kappa h). \quad (2)$$

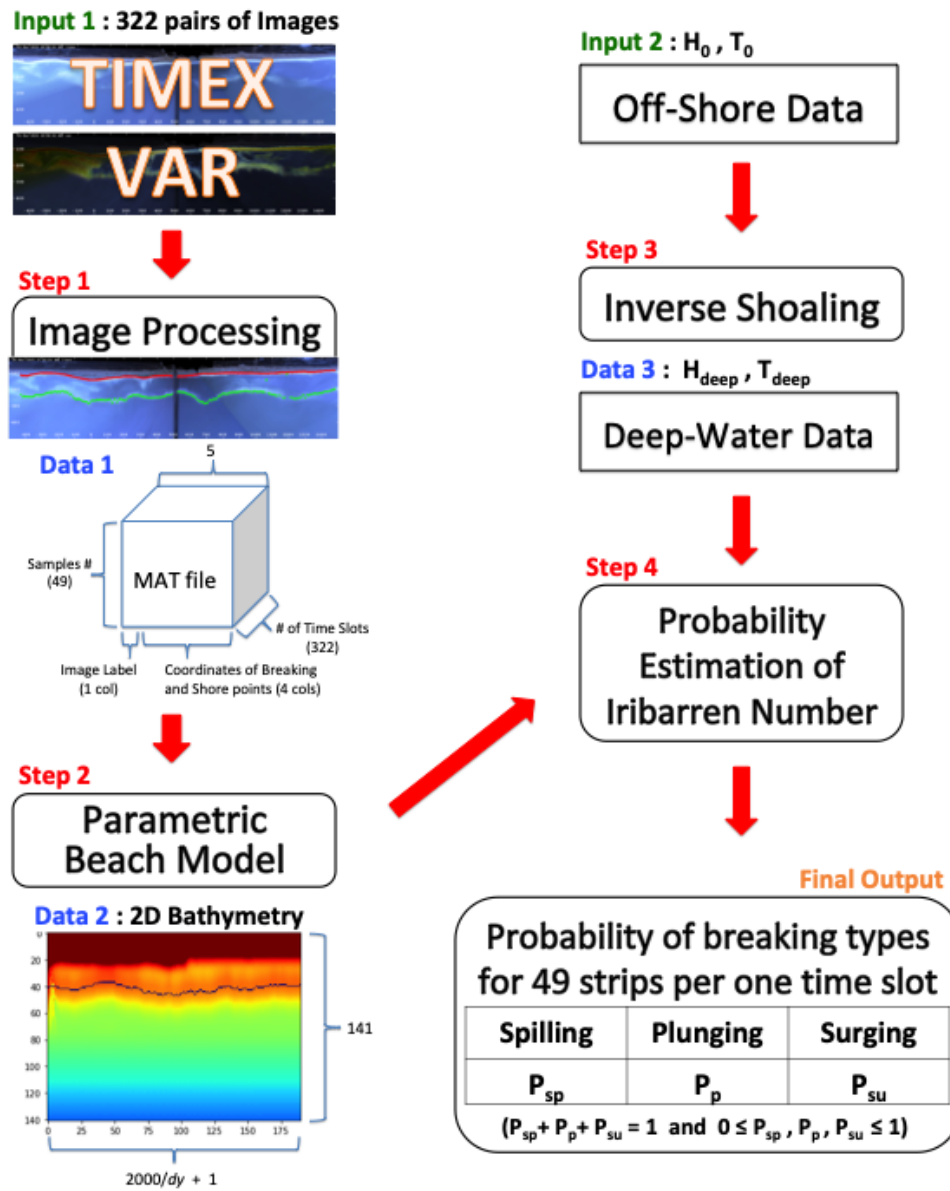


Figure 4: Flowchart of the direct approach

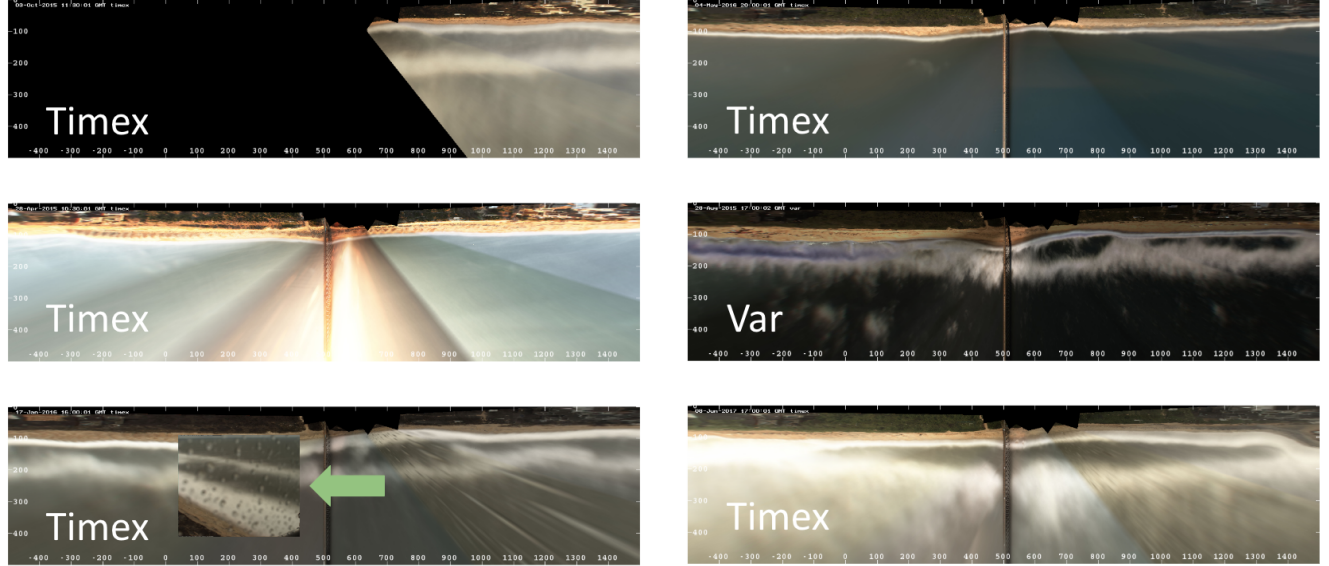


Figure 5: The examples of unsuitable images. Each image is labeled according to the type. From left to right, they correlate to the image requirements list starting from number 2.

### 3.1 Direct Approach

The Figure 4 outlines the flow of the first approach.

First, the TIMEX and VAR images of the surfzone are input into an image processing tool to identify the shoreline and sand bar locations. These locations are passed into a tool (described below in step 2 of this approach) that solves an inverse problem to calculate the bathymetry of the beach. Finally, the bathymetry is used to approximate a slope at the breaking point and offshore wave conditions in order to classify the wave type using the Iribarren number.

#### Step 1: Image Data Cleaning and Processing

Approximately 6000 TIMEX and VAR images ranging from 2015 to 2017 were downloaded from the Oregon State University Coastal Image Lab. Unfortunately, not all the downloaded images were suitable for the purpose of this study. The requirements of the image data are:

1. Both TIMEX and VAR images must be available at the same time and day.
2. The entire range of image must be present.
3. There must be distinct evidence of wave breaking in the image.
4. The TIMEX images cannot have glares.
5. The VAR images must have a black shore.
6. There should not be any light beam pattern in the image.

Most of the suitable images were from the months of January through May and December, and the best times to sample the images were from 10 am to 4 pm EDT (see Figure 6). In general, the images from June through November usually did not contain any breaking waves or had too much noise, and the images from outside of the peak sample time range were usually too dark or bright to process. Out of about 6000 downloaded images, only 644 images met the requirements above. Recall that both TIMEX and VAR images were being used to extract the shorelines and breaking points, which yields a total of 322 images of usable

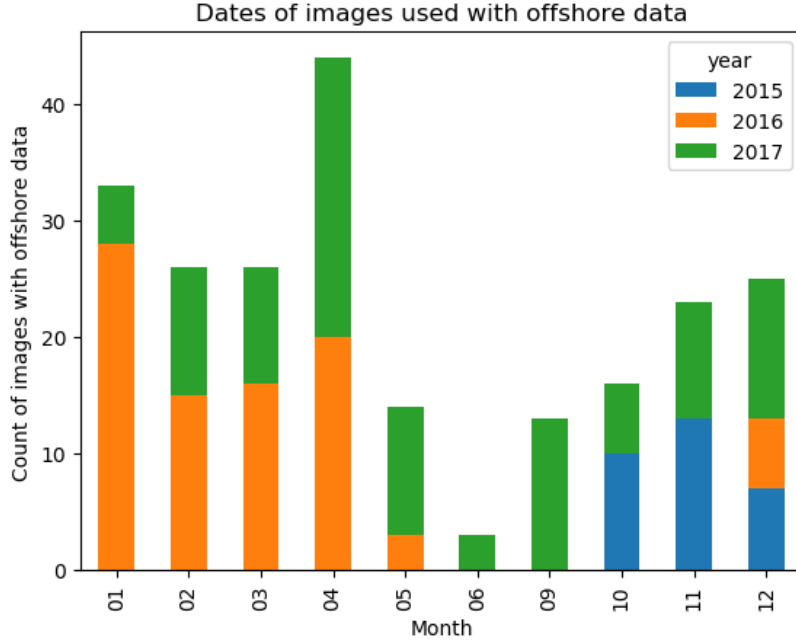


Figure 6: Example dataset of image counts used for model training by month and year. No images from July or August were selected in the set.

data with `RemoveSingle.m`, `RemoveGlare.m`, and `RemoveCameraDead.m`. Some unsuitable images were able to be screened. However, not all images were screened automatically because each case has different pattern in its image while the others are hard to extract their pattern numerically.

From the suitable images, the coordinates of the shoreline and breaking point need to be extracted in order to estimate bathymetries. This can be done by detecting the two local maxima of the intensity per column of the gray-scaled TIMEX or VAR image. The algorithm is described below in Algorithm 1.

---

**Algorithm 1** Detecting shore line and breaking points from a pair of TIMEX and VAR images ( $292 \times 1263$ )

---

```

1: for  $y=1:1:1263$  do
     $dz(x) = z_V(x+1, y) - z_V(x, y)$ 
     $x_s = \arg \max_{\tau_s \geq x} dz(x)$ 
     $\bar{z}(x, y) = \min(z_T(x, y), z_V(x, y))$ 
    Solve Eq.(3)
2: end for
```

---

The images are first converted to gray-scale for low cost computation from RGB type, then they are cropped to remove labels and missing pixels. Let  $x$  be vertical coordinate from the top in an image and the horizontal coordinate of the searching slide where the bar goes from left to right to search (the second plot of Figure 7),  $y$  be the horizontal coordinate of shoreline and bar in an image, and  $z_T, z_V$  be the intensities of the TIMEX and VAR images, respectively. After cleaning the images further, the coordinates of the shoreline and sand bar,  $y$ , are found by browsing slide intensity function values,  $z_T$  and  $z_V$  with respect to  $x$ . Since VAR images have zero intensity,  $z_V$ , above the shoreline (upper white region), those areas should be pitch black. The coordinates of the shoreline is obtained when the intensity of VAR image reaches its first maximum difference in intensity (See Algorithm 1); this happens at the white area in the VAR image. Note that  $x$  goes from top to bottom of the VAR image, however this does not work when the VAR image has noise. Finding the breaking point coordinates is more challenging than the shore line coordinates as there are likely to be more than one local maximum intensity after shoreline. Normally, the outer bottom edge of white lower region is estimated as the breaking points, because the foam starts emerging from the breaking points which appears

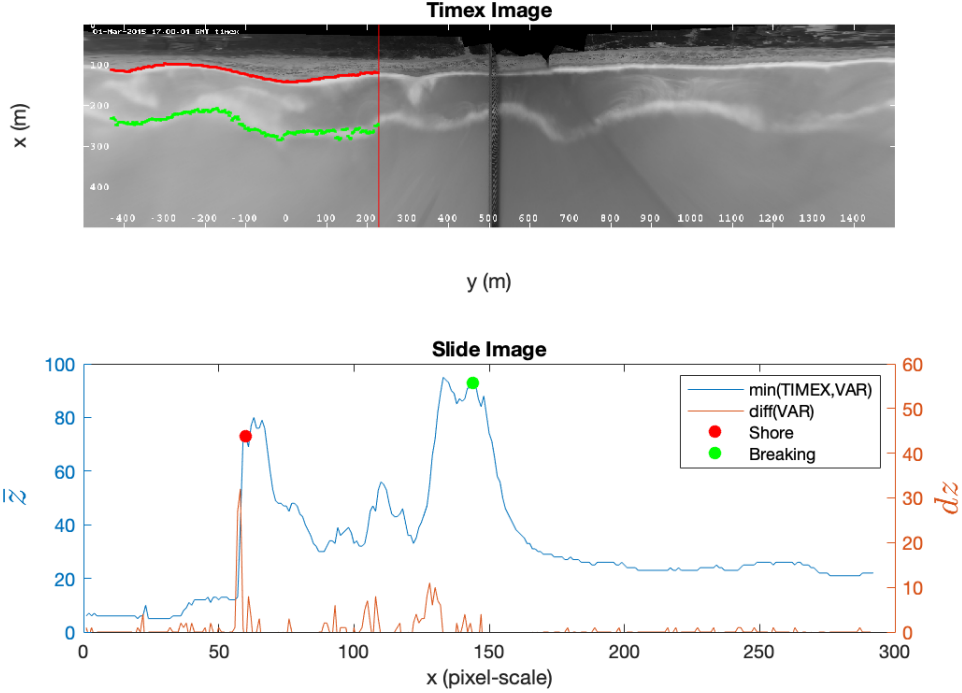


Figure 7: The top figure shows gray-scale image and shore (red) and breaking point (green) column-wise. The bottom plot shows the slide of VAR image and slide of  $\min(\text{TIMEX}, \text{VAR})$  along the red vertical line in the top figure.

in white as well. Consider the following objective function to obtain the most appropriate breaking point by adding a penalty term and modifying the area of trapezoid,

$$x_b = \arg \max_{x \geq x_s} \left( \frac{\bar{z}(x, y_b) + \bar{z}(x_s, y_s)}{2} \right) \log(x) + \log \left( \frac{x - x_s}{75} \right) \quad (3)$$

where  $y_b = y_s$  in the same column,  $\bar{z} = \min(z_T(x, y), z_V(x, y))$ ,  $(x_s, y_s)$  is the shoreline coordinate,  $(x_b, y_b)$  is breaking point coordinate, and  $\bar{z}$  is the intensity defined in Algorithm 1 (see Figure 7).

### Step 2: Bathymetry and Slope Estimation

Recall that using the Iribarren number requires knowing the beach slope,  $m$ . There is a parametric beach tool, provided by USACE, that finds the 2D bathymetry based on the work of Holman *et al.* [8].

Using this, the bathymetry is estimated by sampling 49 1D cuts along the seaward direction of each image. These cuts allow to account for changes in the bathymetry along the coastline in a simple way. Figure 9 illustrates several of these bathymetry profiles.

The slope is calculated right before the breaking point and then used in Iribarren's formula. Specifically, the maximum slope over an interval of 100 meters prior to the breaking point is selected as the slope of each bathymetry profile.

### Step 3: Inverse Shoaling and Dispersion Relation

Although the wave height and period data at shallow water (from between 6 and 11 meters in depth) is available, the wave information at deep water is the actual data required as an input for (1). Henceforth, the wave data measured at the water depths of 100 meters or more will be considered as deep water. A procedure to

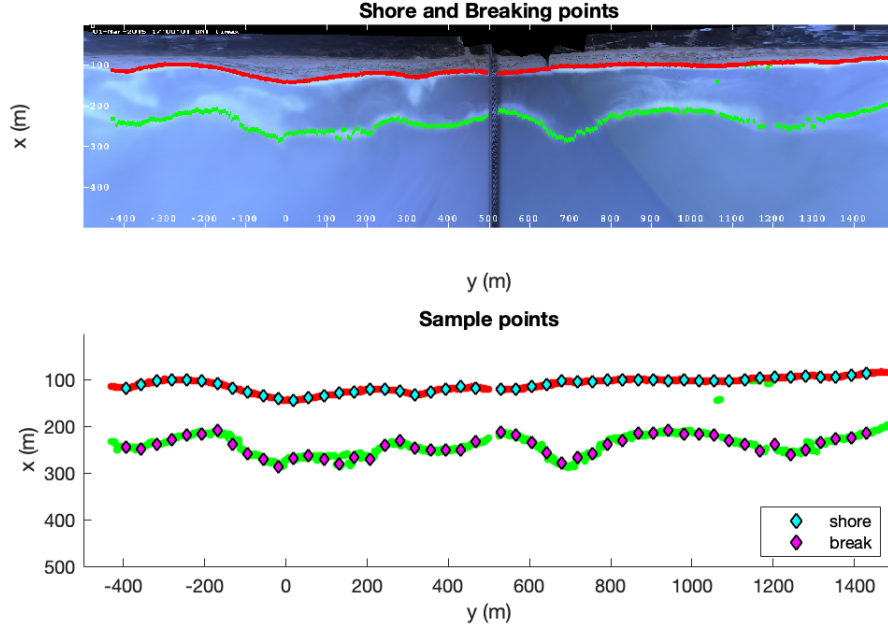


Figure 8: After the step in Figure 7, the shoreline (red) and the breaking points (green) are obtained. From the acquired points, the sample points were selected evenly.

calculate the wave height and length at these locations, using data at shallow water as inputs, is now described.

The following are defined for the computations in this section. A  $d$  subindex denotes data in deep water:

- $H$  Shallow water wave height (Known information)
- $L$  Shallow water wave length (Computed from the dispersion relation)
- $h$  Shallow water depth (Known information)
- $T = T_d$  Wave period (Known information)
- $H_d$  Deep water wave height (Computed from inverse shoaling)
- $L_d$  Deep water wave length (Computed from the dispersion relation)
- $h_d$  Deep water depth (Known information)

Recall, the dispersion relation in equation 2 is

$$\sigma^2 = g\kappa \tanh(\kappa h)$$

where

$$\sigma = \frac{2\pi}{T}$$

and

$$\kappa = \frac{2\pi}{L}.$$

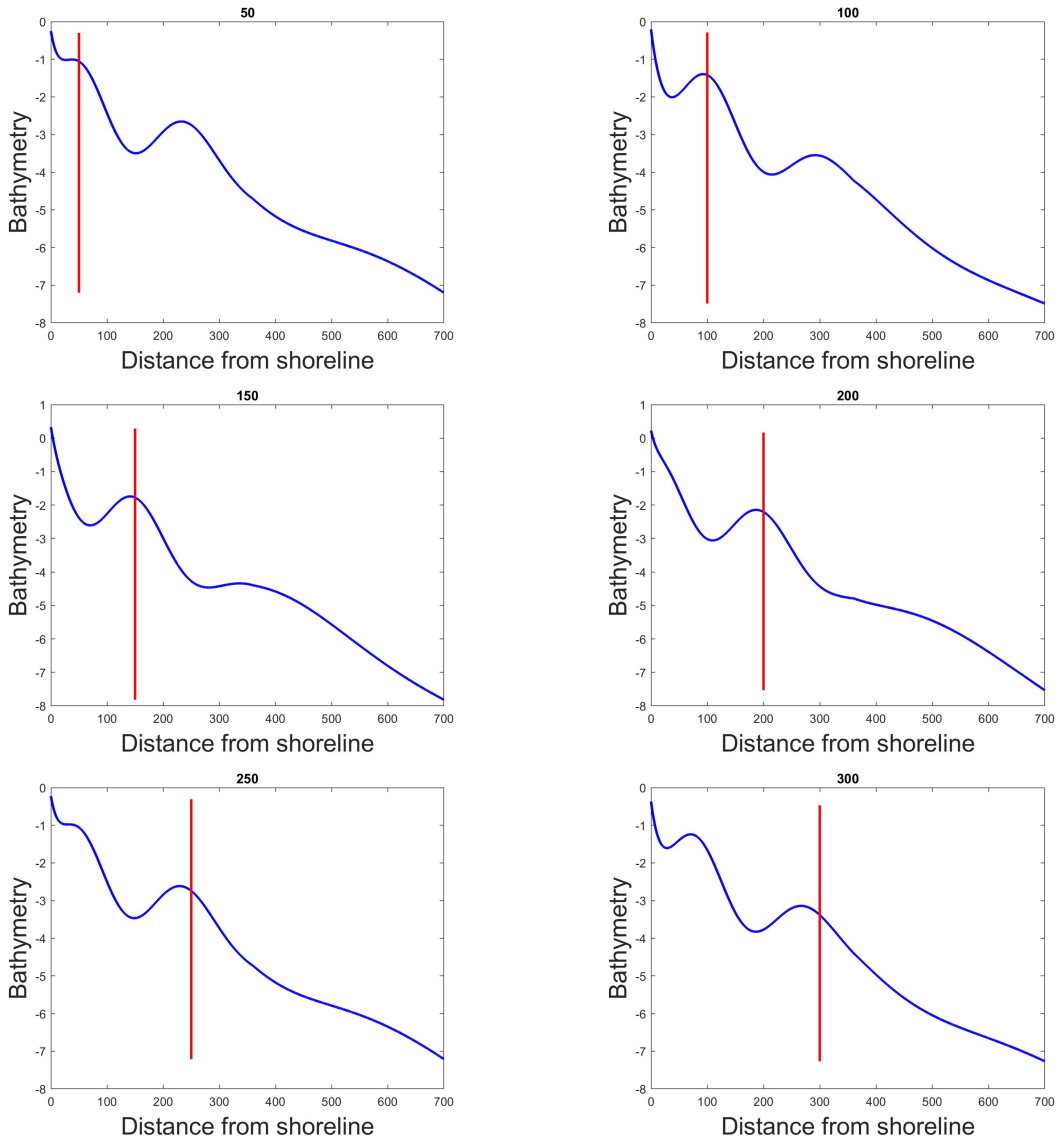


Figure 9: Bathymetry examples with varying distances from shore.

First, we can find  $L$  and  $L_d$  using the dispersion relation. Below is the explanation to find  $L_d$ . The computation for  $L$  is similar.

$$\left(\frac{2\pi}{T_d}\right)^2 = g \left(\frac{2\pi}{L_d}\right) \tanh\left(\frac{2\pi}{L_d} h_d\right)$$

Using linear wave theory, it is assumed that the period is constant, [11] hence  $T = T_d$

$$\left(\frac{2\pi}{T}\right)^2 = g \left(\frac{2\pi}{L_d}\right) \tanh\left(\frac{2\pi}{L_d} h_d\right).$$

When  $h_d$  is known, the only unknown in the equation is  $L_d$ , which can be solved by using any numerical method for nonlinear equations. In this work, an initial guess using the deep water approximation of

$$L_d \approx \frac{g}{2\pi} T_d^2, \quad (4)$$

was used. Notice that this approximation is the large limit of the dispersion relation (see equation 2) as  $h \rightarrow \infty$ .

Now to find  $H_d$ , the conservation of energy flux [2] requires

$$\frac{dEC_g}{dx} = 0, \quad (5)$$

where

$$E = \rho g H^2 / 8$$

is the wave energy,  $\rho$  is density,  $c_g$  is the group celerity, and  $g$  is the acceleration due to gravity.

From this conservation law,

$$\begin{aligned} EC_g &= E_d C_{g_d} \\ \Rightarrow \frac{1}{8} \rho g H^2 C_g &= \frac{1}{8} \rho g H_d^2 C_{g_d} \\ \Rightarrow H^2 \frac{1}{2} \frac{L}{T} \left(1 + \frac{\frac{4\pi h}{L}}{\sinh(\frac{4\pi h}{L})}\right) &= H_d^2 \frac{1}{2} \frac{L_d}{T_d} \left(1 + \frac{\frac{4\pi h_d}{L_d}}{\sinh(\frac{4\pi h_d}{L_d})}\right) \\ \Rightarrow H_d &= \left[ \frac{H^2 \frac{1}{2} \frac{L}{T} \left(1 + \frac{\frac{4\pi h}{L}}{\sinh(\frac{4\pi h}{L})}\right)}{\frac{1}{2} \frac{L_d}{T_d} \left(1 + \frac{\frac{4\pi h_d}{L_d}}{\sinh(\frac{4\pi h_d}{L_d})}\right)} \right]^{1/2} \\ \Rightarrow H_d &= \left[ \frac{H^2 L \left(1 + \frac{\frac{4\pi h}{L}}{\sinh(\frac{4\pi h}{L})}\right)}{L_d \left(1 + \frac{\frac{4\pi h_d}{L_d}}{\sinh(\frac{4\pi h_d}{L_d})}\right)} \right]^{1/2}, \end{aligned}$$

which can be directly computed. Above, the group celerity

$$C_g = \frac{1}{2} \frac{L}{T} \left[ 1 + \frac{\frac{4\pi h}{L}}{\sinh(\frac{4\pi h}{L})} \right]$$

was used as well as  $T = T_d$  from linear wave theory [11].

Without Inverse Shoaling	Spilling Slope (Degrees)	Plunging Slope (Degrees)	Surging Slope (Degrees)
Min	[0, 0.98)	[0.98, 6.45)	[6.45, 90)
Max	[0, 7.48)	[7.48, 40.91)	[40.91, 90)
Average	[0, 3.19)	[3.19, 20.22)	[20.22, 90)

Table 2: Estimated slopes needed for each wave breaker type based off of 19,525 wave data collections at Duck, NC from 2015-2018.

With Inverse Shoaling	Spilling Slope (Degrees)	Plunging Slope (Degrees)	Surging Slope (Degrees)
Min	[0, 0.52)	[0.52, 3.44)	[3.44, 90)
Max	[0, 7.29)	[7.29, 40.16)	[40.16, 90)
Average	[0, 2.82)	[2.82, 18.03)	[18.03, 90)

### 3.1.1 Inverse Shoaling vs. Non-Inverse Shoaling Analysis - To Inverse Shoal or Not to Inverse Shoal

In Duck, NC, a research is being conducted to collect data in order to better understand the ocean wave dynamics. In this section, the results of offshore data from 2015-2018 are examined in order to better understand the behavior and distributions of offshore wave height,  $H_o$  and offshore wave length,  $L_o$ . Since these values are used to calculate the Iribarren number,  $I$  and  $H_o$  information provides a way to analyze the bathymetry necessary to create each wave type (see table 1).

As waves get closer to shore, they are affected by a process called shoaling. Shoaling occurs when waves “feel” the ocean floor and begin to grow in height. As a result of the conservation of wave energy flux and the dispersion relation (equation 4), they develop a smaller wavelength while they change in height. Shoaling provides a more accurate way to compute  $L_o$  than using the deep water approximation to the dispersion relation.

Note that the data collected was waveTp (Peak Spectral Period) and waveHs (Significant Wave Height) from an 11m AWAC sensor. In order to gather offshore information, the AWAC takes samples over approximately 22 minute intervals.

We see in Table 2 the differences between the inverse shoaling and non-inverse shoaling methods and the effect on the slope of bathymetry required for each breaker type. The slopes were found by solving the Iribarren formula using the cutoff Iribarren number for each breaker type (0.5 for plunging and 3.3 for surging) as well as using the offshore data from the 11m AWAC.

$$I = \frac{m}{\sqrt{\frac{H_o}{L_o}}}$$

$$m = I \sqrt{\frac{H_o}{L_o}}$$

$$\text{slope angle} = \arctan \left( I \sqrt{\frac{H_o}{L_o}} \right)$$

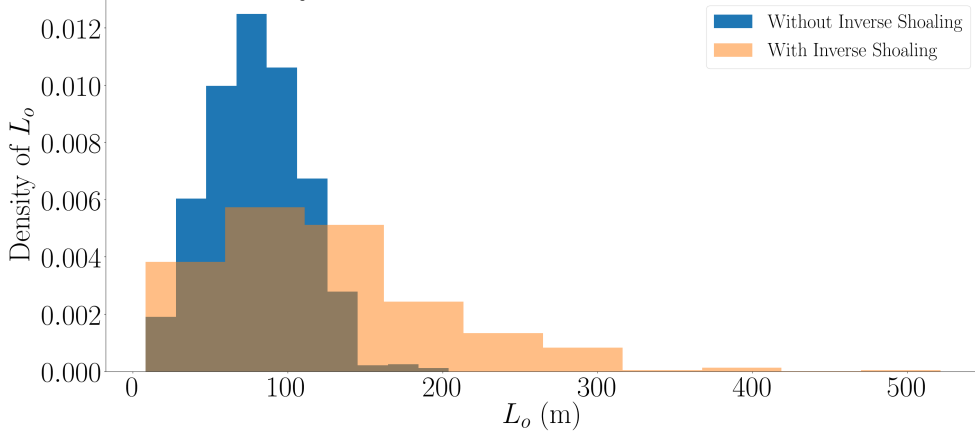
See Figure 10 and 11 for a comparison of the distributions and analysis of the differences of the offshore data with and without inverse shoaling.

#### Step 4: Calculating the Frequency of Expected Breaking Types

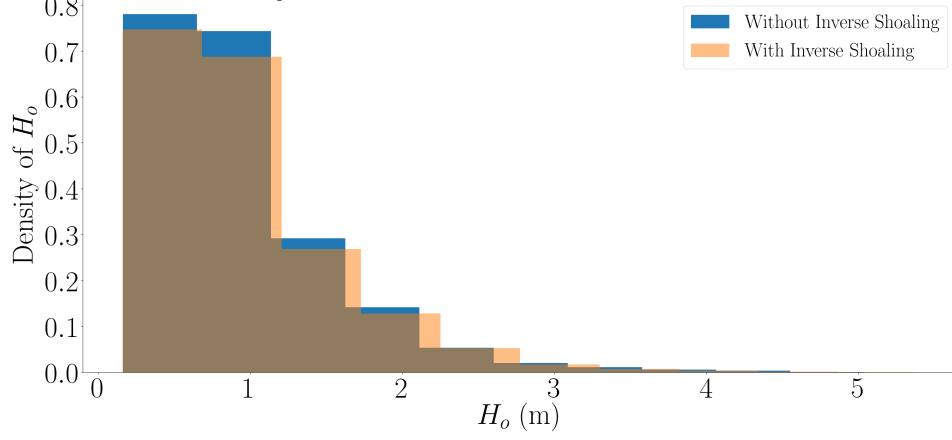
In practice, the variability in height and period of each individual wave coming to shore is to be expected. This variability implies that a range of different Iribarren numbers should be estimated in order to make any reasonable breaker type classification. A straightforward application of the Iribarren formula (1) with the average values of  $H_o$  and  $L_o$  is not enough to quantify this variability.

The frequency distributions for the observed height from the observed deep water wave heights obey a

Probability Distribution of  $L_o$  at Duck, NC  
for years 2015-2018: 11 m AWAC data



Probability Distribution of  $H_o$  at Duck, NC  
for years 2015-2018: 11 m AWAC data



Probability Distribution of  $\sqrt{H_o/L_o}$  at Duck, NC  
for years 2015-2018: 11 m AWAC data

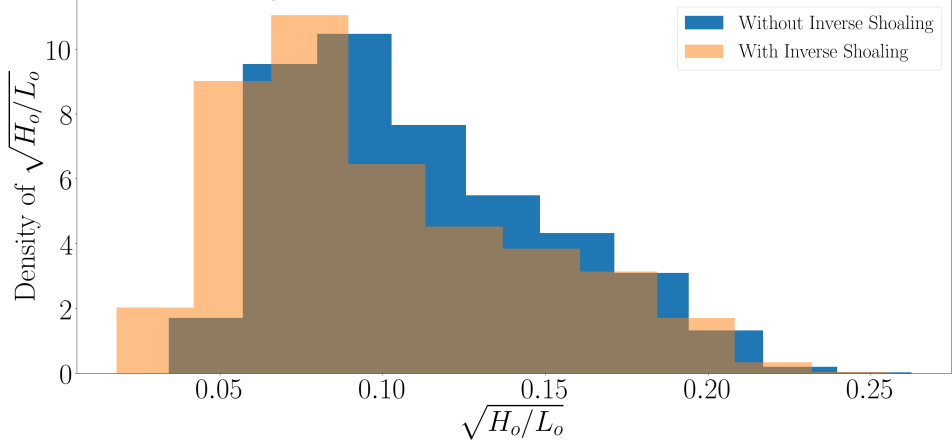
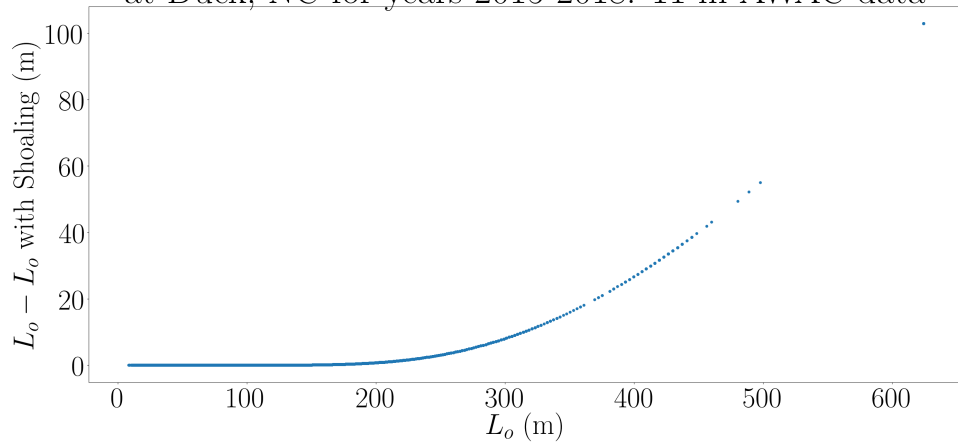
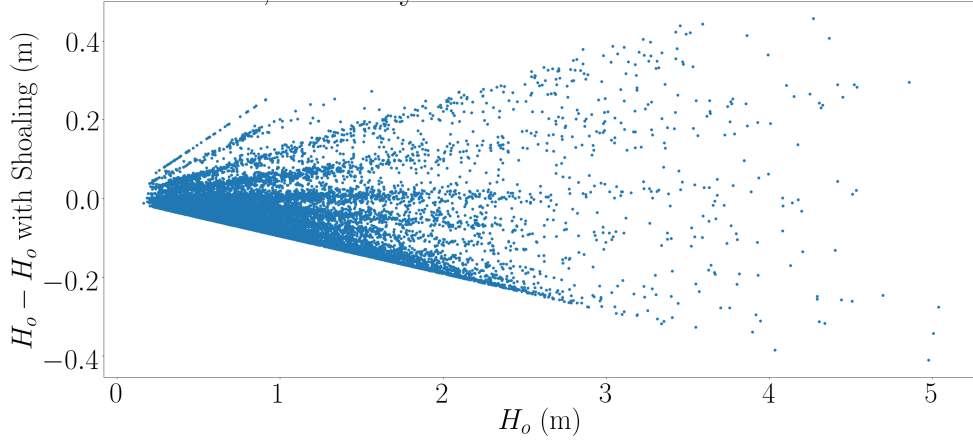


Figure 10: Distributions of offshore data  $L_o$ ,  $H_o$ , and  $\sqrt{\frac{H_o}{L_o}}$  respectively using 19,525 data points. The blue bars represent the probability distribution without inverse shoaling, and the transparent orange bars represent the same but with inverse shoaling. The brown region is the overlapping area between two probability distributions.

Computing  $L_o$  with Shoaling Vs. Non-Shoaling  
at Duck, NC for years 2015-2018: 11 m AWAC data



Computing  $H_o$  with Shoaling Vs. Non-Shoaling  
at Duck, NC for years 2015-2018: 11 m AWAC data



Computing  $\sqrt{H_o/L_o}$  with Shoaling Vs. Non-Shoaling  
at Duck, NC for years 2015-2018: 11 m AWAC data

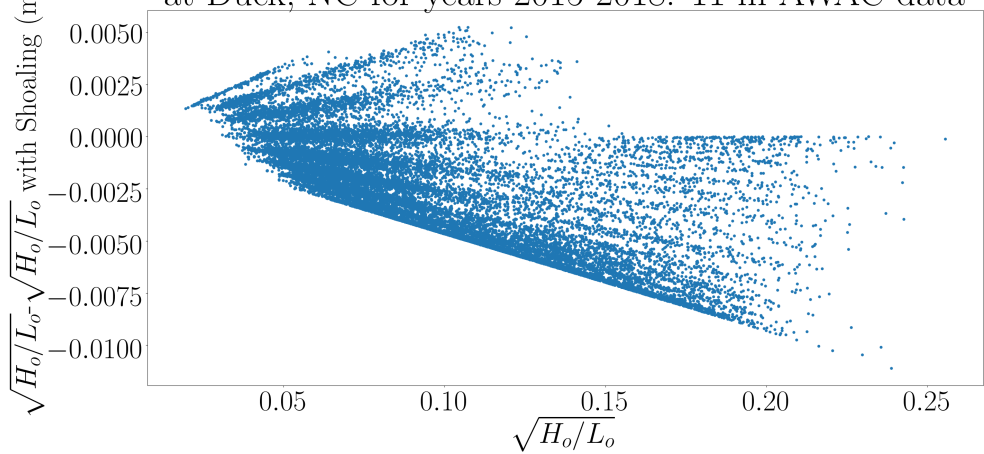


Figure 11: Difference graphs of wave characteristics used in the Iribarren calculations. The shoaling affects the wave length, wave period, and the denominator of the Iribarren formula.

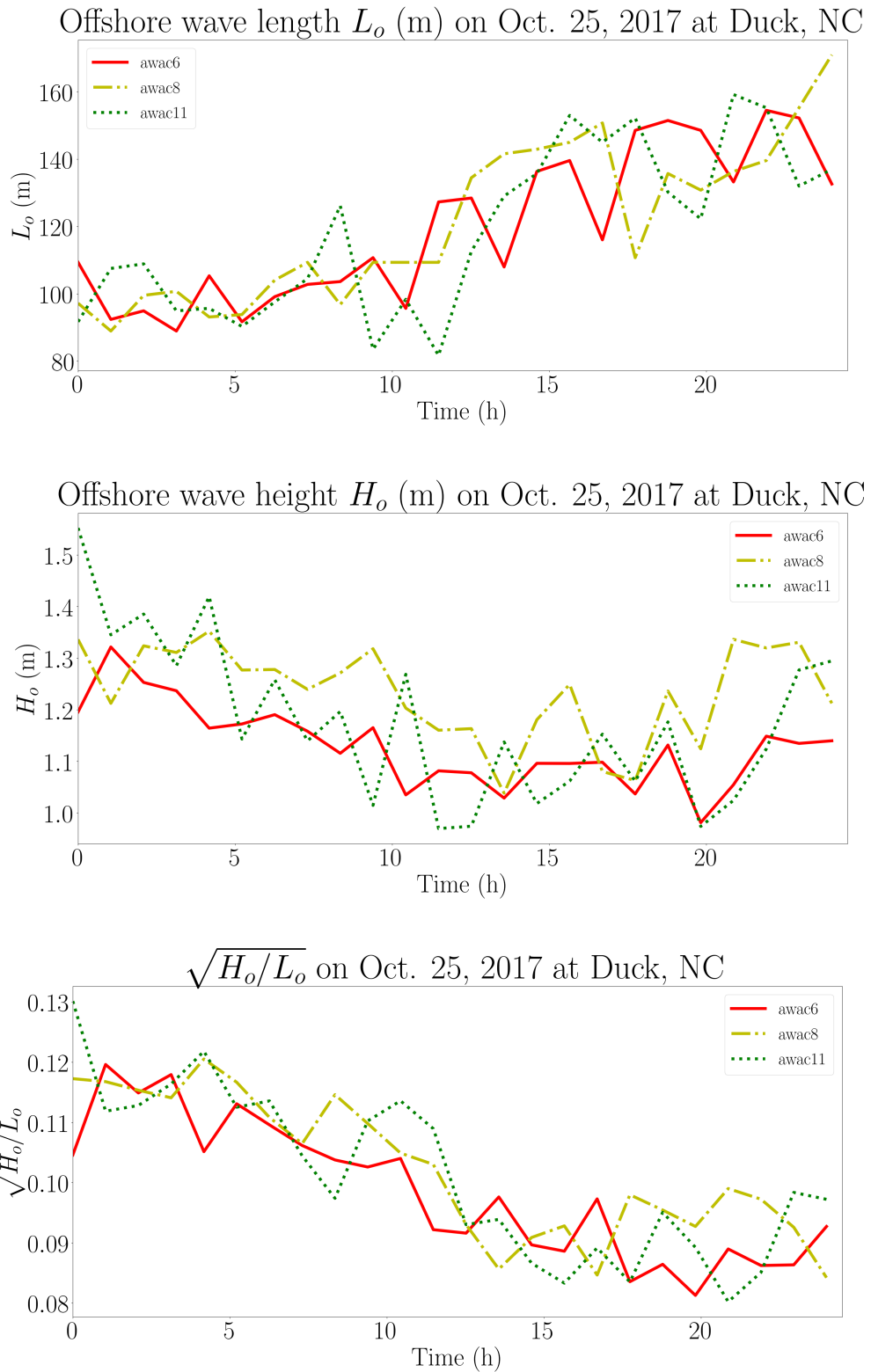


Figure 12: Data from Oct 25 at Duck, NC over the course of 24 hours from different AWAC monitor depths.

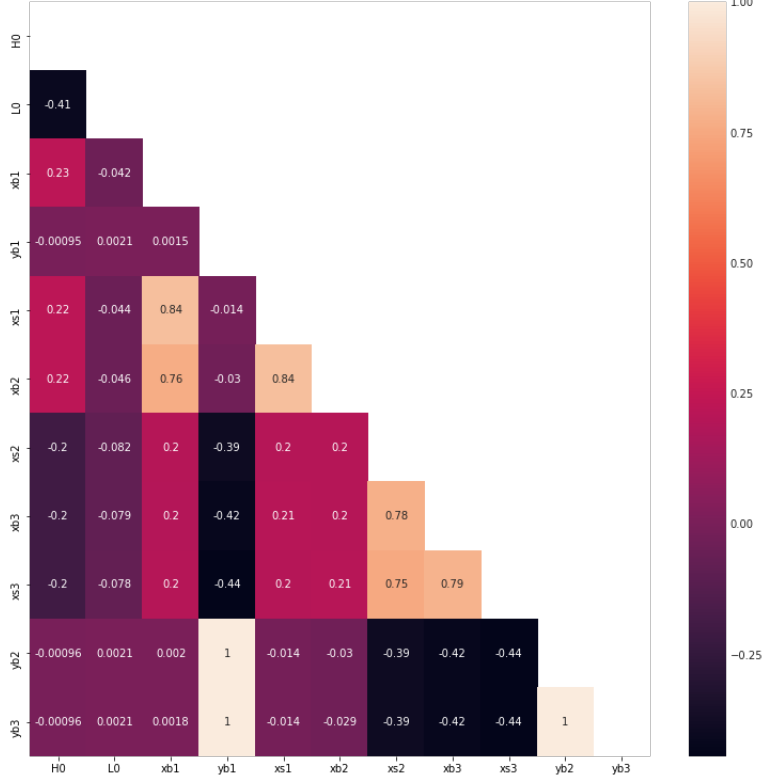


Figure 13: Heatmap showing the correlation between 12,131 rows of data used to train and test the model.

Rayleigh distribution with density function [1, 12],

$$f(x; \sigma) = \frac{x}{\sigma^2} e^{-\frac{x^2}{2\sigma^2}}$$

which can be entirely characterized by its mean. The Iribarren number calculations for this study do not introduce variance for this quantity as no reference to a frequency distribution is available. Due to this, the inverse shoaling procedure is used to calculate the wave height average at deep water, and this value is used as the mean of the wave height distribution. A Monte Carlo simulation is followed by picking 10,000 random height values based on this distribution, and as a result, 10,000 Iribarren numbers are correspondingly calculated. The Table 1 is used again to classify these numbers, and then, the percentages of each expected breaking type are calculated. These calculated percentages are interpreted as the probabilities of observing each breaking type along each 1D bathymetry strip.

### 3.2 Machine Learning Approaches

As described above, the direct approach of breaker type classification requires imagery data pre-processing, the bathymetry and its slope estimation, inverse shoaling for the deep water wave properties with Monte Carlo simulation, and calculation of the Iribarren number. To gain higher computational efficiency and more knowledge on the relationship between the imagery data and the breaker types, the machine learning approaches to classify wave breaker types based on breaking points were explored. The wave breaker type in the direct approach is uniquely determined by the bathymetry and offshore wave height and wave length. Moreover, the bathymetry is simulated with the coordinates of the breaking points and shoreline. Therefore, these coordinates together with the offshore wave conditions are sufficient to determine the wave breaker type. Based on this, a machine learning approach is proposed and tested to accelerate the direct method.

In this machine learning approach, the imagery data is pre-processed to identify the breaking points and shoreline coordinates. Then, the offshore wave height and period information will be collected and processed

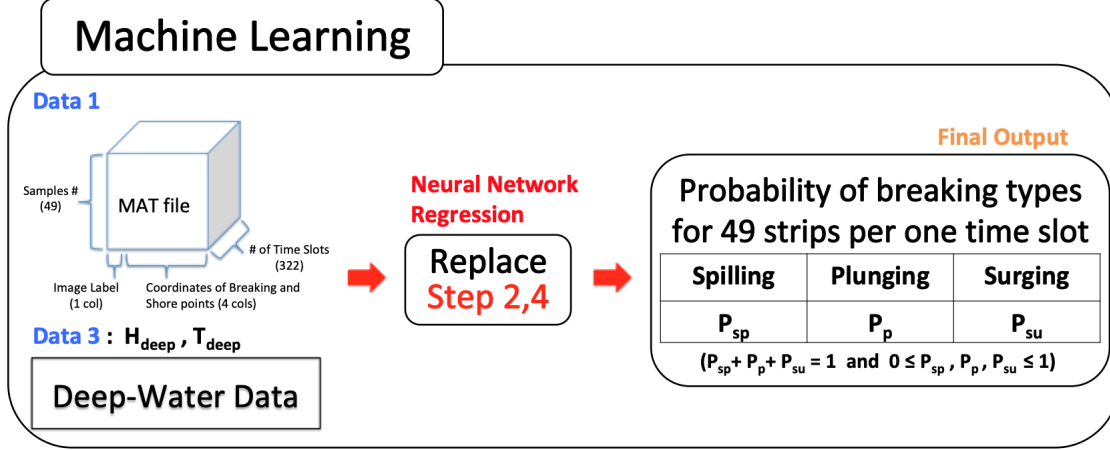


Figure 14: Machine Learning step of the study. This follows from Figure 4.

by the inverse shoaling to get the deep water wave height and length. With these inputs, a surrogate model will obtain the the probability of each breaker type. The processes avoided by the this machine learning approach are shown in Figure 14.

Note that the breaker type is obtained for each cut of the image as mentioned in section 3.1. Each cut of the image corresponds to one set of breaking point and shoreline coordinates  $\{x_b, x_s, y_b, y_s | y_b = y_s\}$ . The direct method used to classify breaker type depends on the local bathymetry. The reason behind cutting the images into 1D strips and predicting the label of each cut is that the bathymetry of each strip is calculated locally. Although there is correlation of bathymetry in the whole image, the further from the cut, the lower influence gets when determining the bathymetry at a certain cut.

The 49 1D cuts correspond to 49 sets of breaking and shoreline coordinates. To include some spatial correlation, the coordinates of these cuts' two closest neighbours are also included as the input of the surrogate model for the prediction of the breaker type at each cut. The output of the model then consists of three values corresponding to the probability of each breaker type. An illustration is shown in the Figure 15. From the strips of 322 images, 12,138 samples are obtained after some data cleaning.

To obtain this surrogate model, Neural Networks, Support Vector Machine Regression, and Random Forest Regression are explored.

### 3.2.1 Neural Networks

Neural Networks were tried as the first surrogate modeling approach for their capability to perform regression tasks. The data set was split into training, validation, and testing sets by the following ratio: (70%, 15%, 15%).

Shown in the Figure 16, the architecture of the best performed Neural Network consists of 2 linear affine layers, where each linear layer is activated by a ReLU activation layer.

Mean square error loss function is used to compare the prediction with the targets.

At the training stage, a  $L_2$  norm regularization term of the Neural Network parameters is added to the loss function to prevent overfitting. The Neural Network was then trained to minimize the loss over the training set. The validation set is used to check the performance of the Neural Network with the mean square error. The best performing Neural Network obtained in this project used SGD optimizer [13], and it has the following structure and hyper parameters:

```

Learning rate: 0.001
regularization weight: 0.001
Optimizer: SGD
Input: 11
Linear Layer: 20 units, ReLU
Linear Layer: 40 units, ReLU
Output: 3
  
```

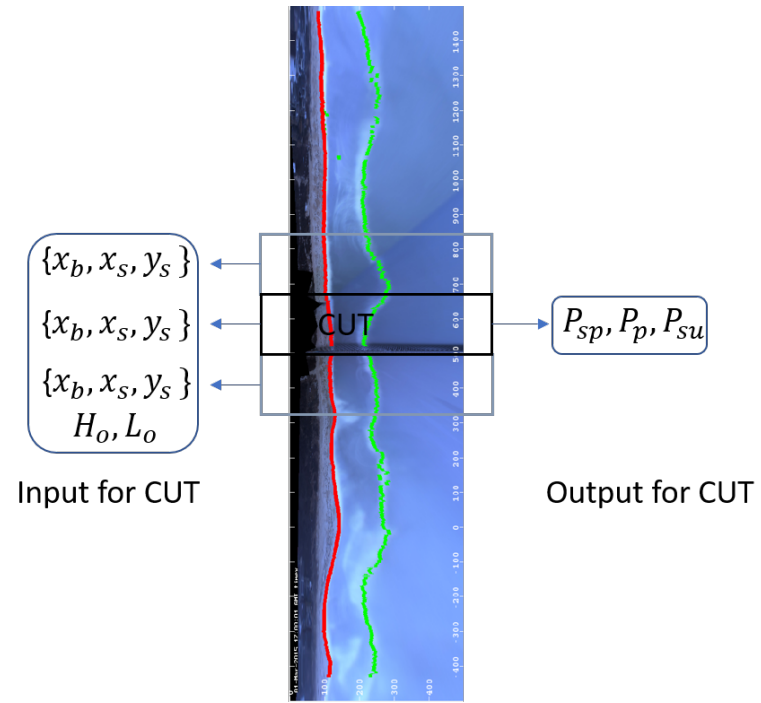


Figure 15: Input and output of the surrogate model

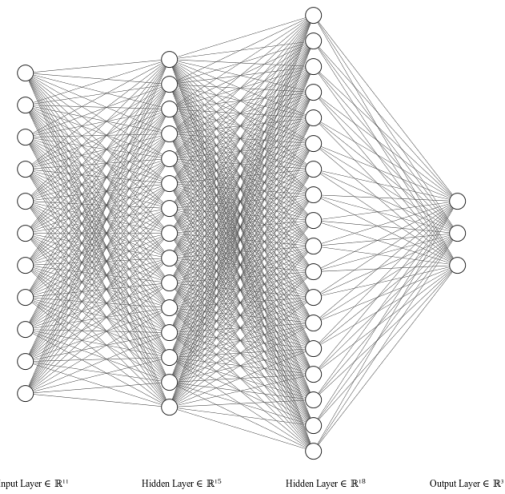


Figure 16: Neural network architecture

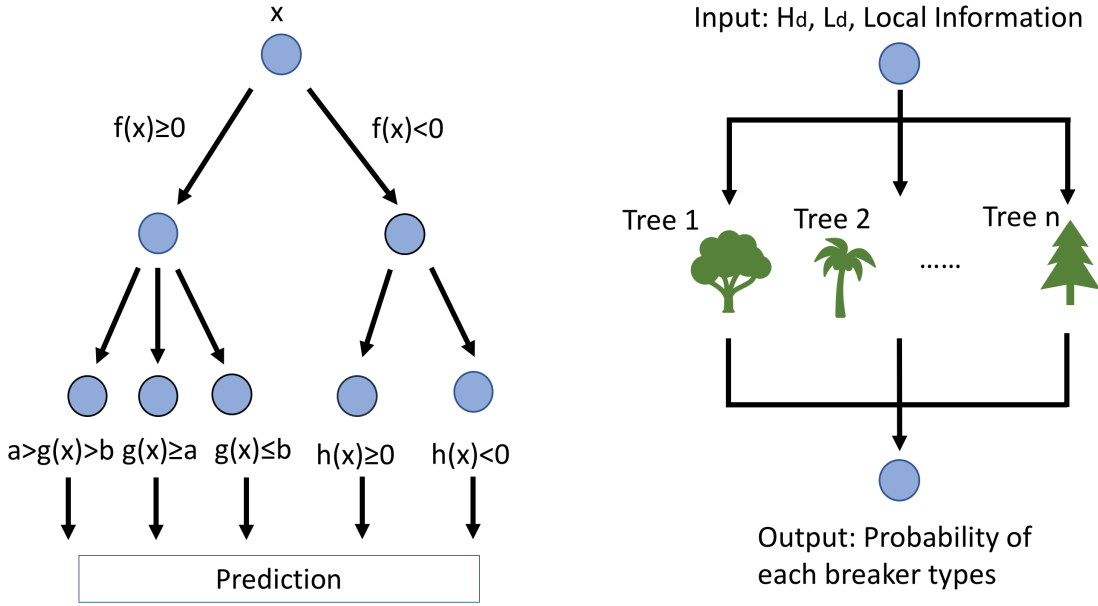


Figure 17: Single Decision Tree

Figure 18: Random Forest with  $n$  Decision Trees

This Neural Network was trained for 1000 epochs to reach the best performance. Google Colab was used for the training with its GPU resource to accelerate the gradient descent, and the training was done in 219.10s.

### 3.2.2 Random Forest Regression

Random Forest is an ensemble learning method based on decision trees. Decision trees are classification and regression models in the form of tree structure. In each decision tree, there are decision nodes and leaf nodes, and each decision node is connected to two or more leaf nodes. Data space is partitioned into several subspace based on the similarities of features. The similarities and partition depends on the metric in feature space. Gini impurity and information gain are widely used metrics. When an observation is put in the tree, starting from the root decision node, it will go through several decision nodes and finally fall into the region where most observations have similar features with it. The prediction result of each observation depends on the fitting results of other observations in the region. More details of decision tree could be found in [14]. Sometimes single decision tree does not work very well due to overfitting and corresponding high variance. Random Forest corrects the decision trees by ensembling several decision trees together. Given a dataset  $\{X_i\}$ ,  $\{1 \leq i \leq N\}$  with corresponding responses  $\{Y_i\}$ ,  $n$  random subsets are taken with replacement. Decision trees are built on these subsets separately with random chosen features. Suppose that test observation is  $\tilde{X}$ , predictions on decision tree  $j$  is  $d_j(\tilde{X})$ , then the prediction result of random forest is

$$f(\tilde{X}) = \frac{1}{n} \sum_{j=1}^n d_j(\tilde{X});$$

which lead to better performance by decreasing the variance of the system. Random Forest regression is used to predict the probability of different wave breaker types. The input and output are the same as the ones in the Neural Network. The only difference is that three random forests are built to predict the probability of the spilling, plunging, and surging waves, and the predictions are normalized to ensure that the sum of predicted probabilities sum to 1.

### 3.2.3 Nonlinear Support Vector Machine Regression

More machine learning approaches are implemented on the same training set. Support Vector Machine Regression (SVR) is a basic machine learning approach for the classification and regression as well. As mentioned in the previous sections, the prediction of probability of different breaker type (spilling, plunging, surging) can be seen as three regression problems. Nonlinear Support Vector Machine could be applied to these problems by transforming input into high dimensional Hilbert space and fitting the function in this space. Given a training set  $\{X_i\}$ ,  $1 \leq i \leq N$  and corresponding responses  $\{Y_i\}$ , Support Vector Machine Regression (SVR) is in the form of [15]

$$f(x) = \sum_{i=1}^N (a_i - a_i^*) G(x_i, x) + b$$

where  $a = (a_1, \dots, a_n)$  is the saddle point which minimizes

$$L(a) = \frac{1}{2} \sum_{i=1}^N \sum_{j=1}^N (a_i - a_i^*)(a_j - a_j^*) G(x_i, x_j) + \epsilon \sum_{i=1}^N (\alpha_i + \alpha_i^*) - \sum_{i=1}^N y_i (a_i - a_i^*)$$

subject to

$$\begin{aligned} \sum_{i=1}^N (a_i - a_i^*) &= 0 \\ \forall i, 0 \leq a_i &\leq C \\ \forall i, 0 \leq a_i^* &\leq C. \end{aligned}$$

$G(\cdot, \cdot)$  is the kernel function, which has multiple choices, like radial basis function Kernel and polynomial kernel. In this project, the radial basis kernel defined by

$$G(\mathbf{x}, \mathbf{y}) = \exp(-\gamma \|\mathbf{x} - \mathbf{y}\|)$$

and is used for SVR regression. In SVR regression, the radial basis function kernel decreases the weights of points that are far away from the predicting point, which make the predicted function value of given point close to the values of its neighbors in the Hilbert space. Maps from the local window of stripes to the probability of three types of waves are predicted by three separate SVR systems. The inputs and outputs are the same as what is defined on Figure 15.

## 4 Evaluation Experiments

The work of Brodie *et al.* contains 5 different frequency observations for the percentage of breaking and non-breaking waves measured at Duck, NC, on October 25th, 2017 between 1 and 4 pm [16]. These observations allow for the following experiments.

1. **Evaluation of the machine learning algorithm compared to the direct approach:** Predictions for beach profiles image and  $H_o$  and  $T_o$  data corresponding to the times and date described above will be calculated via the direct approach and the machine learning approach. These predictions will then be compared.
2. **Comparing estimated and observed breaking wave type frequencies:** On October 25th, 2017, the proportion of spilling and plunging breaking waves were manually classified at five time points for a single location at Duck, NC. Predicted breaking types from the direct approach, the machine learning model will be compared with these observations.
3. **Bathymetry estimate validation:** During October 2015, a bathymetry survey was completed by boat once each week. Image files were available within 12 hours of each reported bathymetry collection. Bathymetry calculated using the parametric beach model on a 141 by 107 grid will be validated against contours based on the interpolated results of this survey.

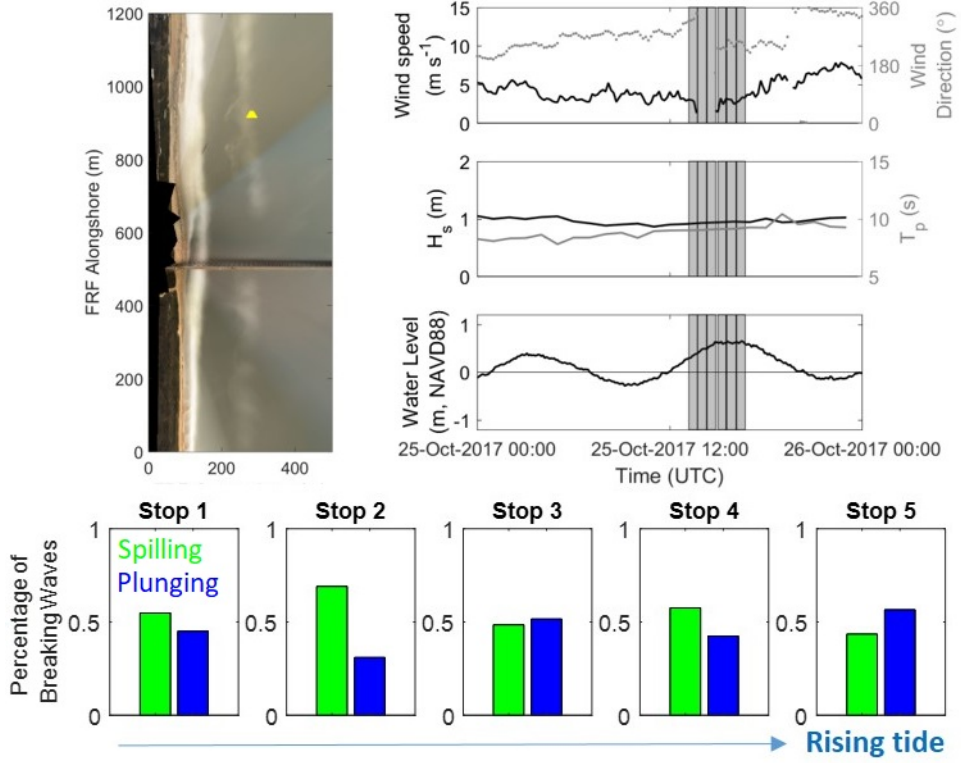


Figure 19: In the upper left, the yellow triangles represent the y-location where the bathymetry and breaking type observations described below were collected. The upper right shows the times at which the observations occurred, and the offshore conditions during that day. The lower part of the figure represents the observed proportions of spilling and plunging waves at each time point (and similar spatial points) [16]

## 5 Results

### 5.1 Comparison of Observed Breaking Types and Estimated Breaking Types

On October 25, 2017, the direct observations of wave types at a position indicated by the yellow triangle in the figure below were measured at five different time points (see Figure 19).

Estimations of bathymetry using Argus imagery from 13.5 hours before and 6.1 hours after these observations were used to estimate breaking types near this spatial point (see Figure 20).

The calculated breaking types based on estimated bathymetry was compared to the manual classifications. About half of the observed waves were plunging and half were spilling during these time periods. Estimates of the probability of plunging are calculated at about 20 m intervals along the shore (see Figure 21).

### 5.2 Comparison of Observed Bathymetry with Parametric Beach Model Result

Observed seabed measurements obtained in October 2015 provide the chance to evaluate bathymetry data produced by the parametric beach model. The comparison between aerial images taken within 12 hours of the reported survey time is shown. These images were not deemed suitable for the described image processing method, so the inputs to the parametric beach model were not available, and the calculated topography could not be compared (see Figure 22).

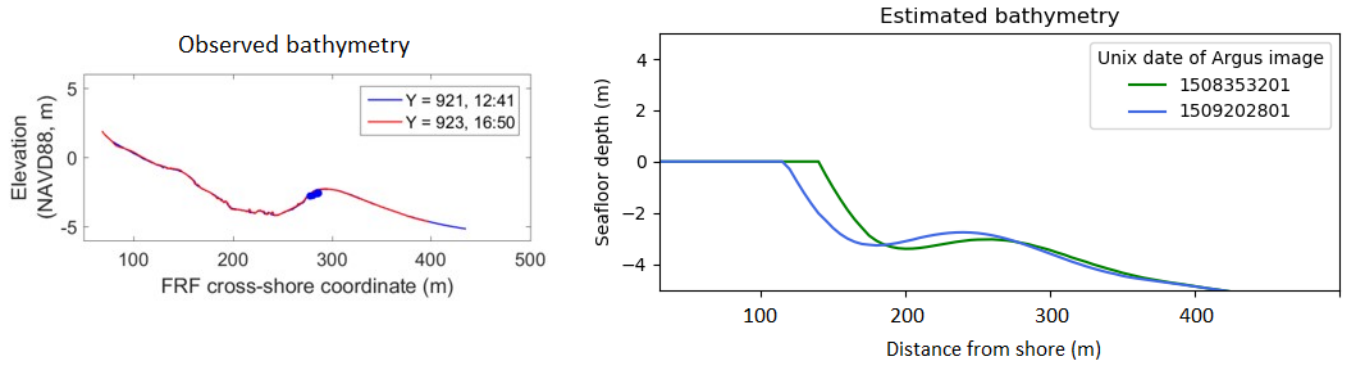


Figure 20: Comparison of predicted and observed [16] bathymetry for Duck NC, October 25, 2017. The sandbar is closer to the shoreline in the estimated instantiation, and the slope from the shore is much steeper. The sandbar is less pronounced in the estimate. However, the results are qualitatively similar.

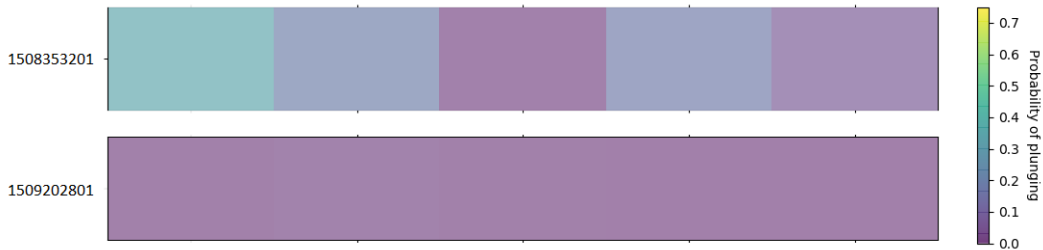


Figure 21: The estimated probabilities of plunging at five intervals around and including the observations of breaking types. The top estimate (which is prior to the known data) is showing a probability of plunging while the bottom estimate (which is after the known data) shows almost no chance of plunging.

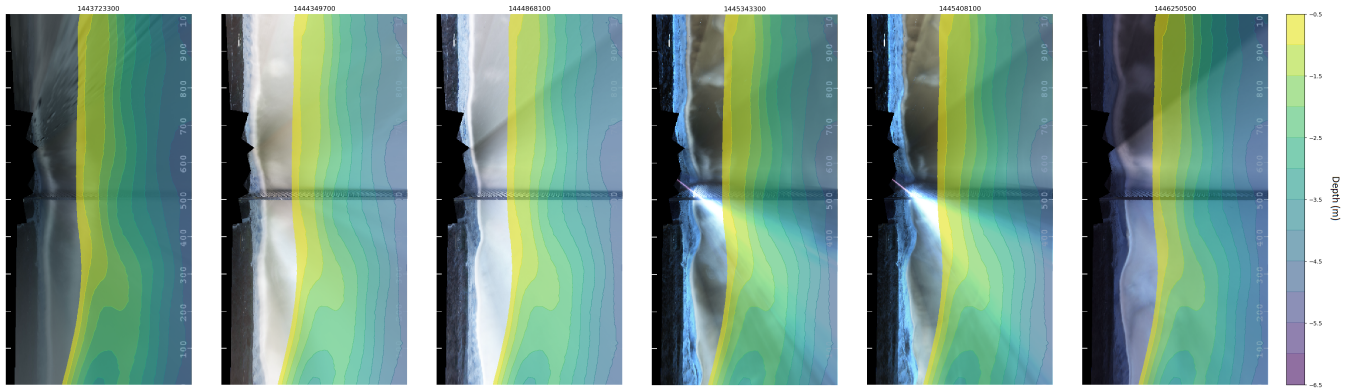


Figure 22: Contour representing the results of bathymetry survey for October 2015 superimposed on Argus image data from within 12 hours of the survey. The title of each image represents the Unix time in GMT.

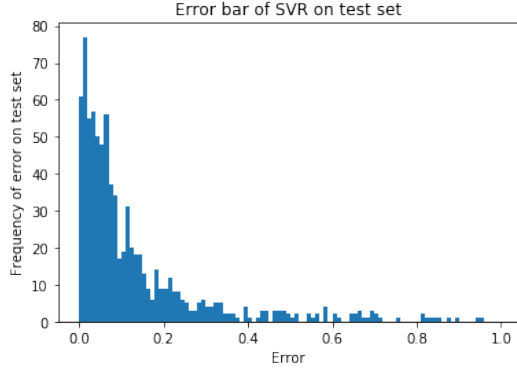


Figure 23: Support Vector Machine Regression

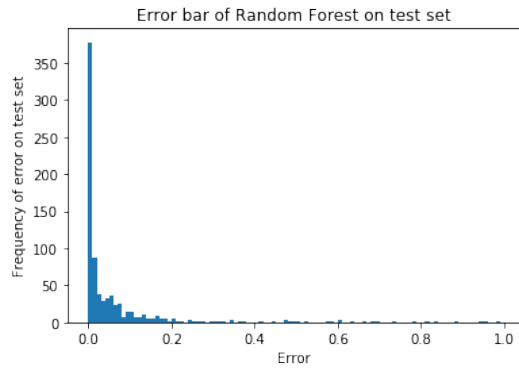


Figure 24: Random Forest

### 5.3 Machine Learning Surrogate Model Performance

To evaluate the performance of the machine learning approaches, prediction of the breaker types on one training data and one test imagery data were produced and shown in Figure 26 and 27. The near shore area was segmented into 49 strips in each image, for each of these strip, a breaker type is predicted. Comparisons between the results of the direct model and multiple machine learning approaches are shown. The color intensity indicates the probability of the existence of plunging wave on the corresponding strip. An overlap of the image with the breaker type prediction is shown in Figure 28 to illustrate.

#### 5.3.1 Neural Networks

With the data set and architecture described in section 3.2.1, the training and validation loss curve of the Neural Network is shown in Figure 25. Although the training and validation loss seem to decrease to a low level, the performance of each prediction task was not as good as that of SVR. The visualization of the prediction on two days is shown in the evaluation section together with that of other surrogate models in Figure 26 and Figure 27. Figure 26 is in the training set and Figure 27 is in the testing set. Note that the prediction at the center of the Figure 26 diverged from the direct method, one possible reason may be the appearance of the pier in the center of the image, and the Neural Network was not able to handle this noise. Further more, the overall performance of the Neural Networks was worse than the random forest and SVR, the reason for this might be the scarcity of training data, the difficulty to tune the hyper parameters, and the choosing of the loss function.

#### 5.3.2 SVR and Random Forest

The training of SVR and Random Forest is efficient. Mean square error bar on test sets (1821 observations) is shown in 5.3.2. Considering the short training time, the result of both methods are encouraging. The comparison of physical model and machine learning methods are shown in Figure 26 and Figure 27.

#### 5.3.3 Modeling Time Comparison

Comparison of modeling time of the two imagery data is shown in table 5.3.3. SVR outpermed all the other methods in terms of modeling time and the accuracy.

Method	Direct Approach	Random Forest	Support Vector Machine Regression	Neural Network
Time(s)	675.48838	0.00671	0.00960	0.02911

Table 3: Modeling time for 2 imagery predictions

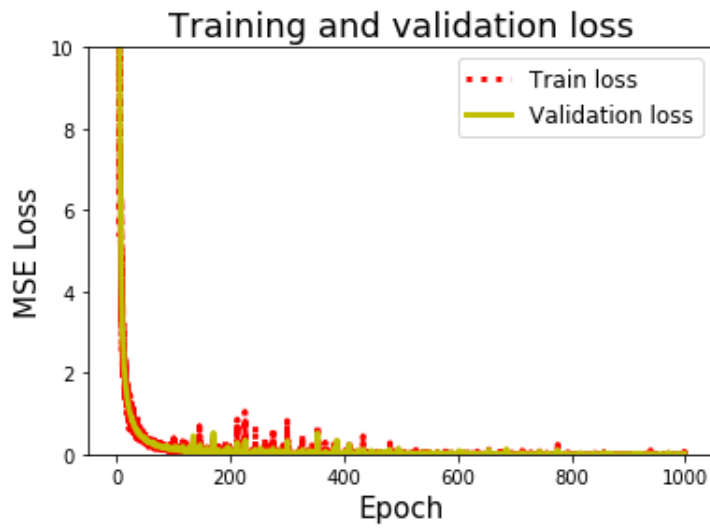


Figure 25: Training and validation loss

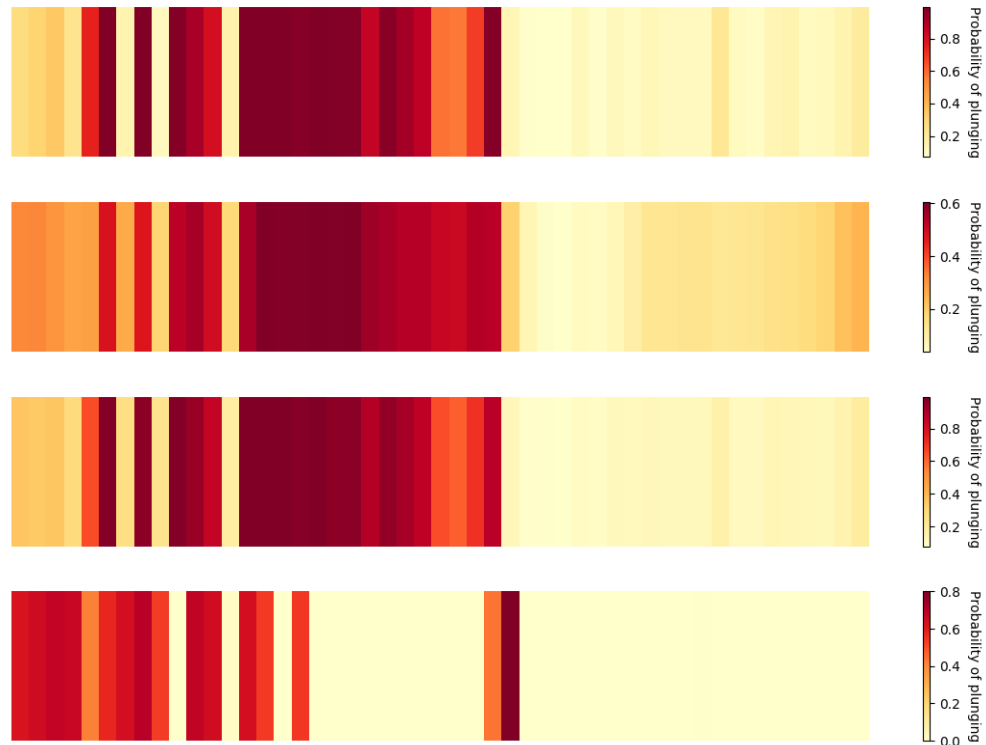


Figure 26: The comparison between the result of training data of direct approach, Support Vector Machine Regression, Random Forest, and Neural Network from top to bottom respectively, using the same image. Darker red represents higher probability of plunging waves in that region.

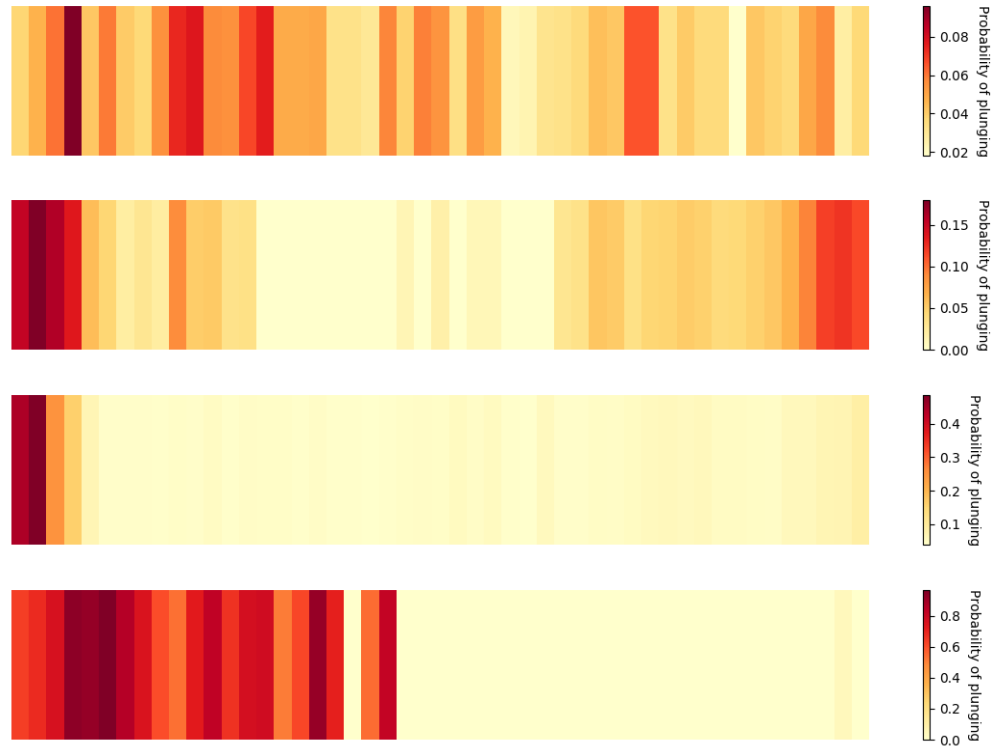


Figure 27: The comparison between the result of test data of direct approach, Support Vector Machine Regression, Random Forest, and Neural Network from top to bottom respectively, using the same image. Darker red represents higher probability of plunging waves in that region.

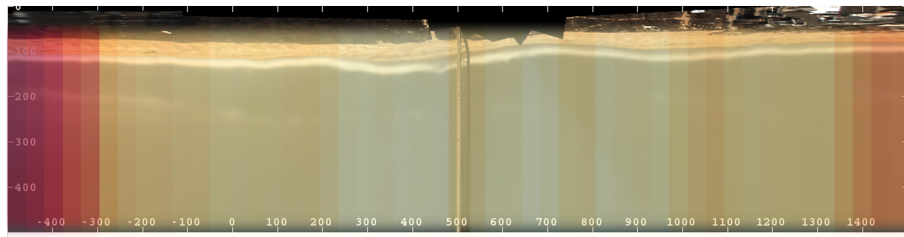


Figure 28: Example of result visualization for a day at Duck, NC. The darker the red, the greater the probability of plunging waves occurring.

## 6 Conclusions and Future Work

In this report, a breaker type classification tool based on the imagery data and offshore wave information is proposed and tested. Note that this task has not been done in the past. The direct method described in section 3.1 receives an imagery of the near shore area, simulates the bathymetry, computes the slope of the seabed at the breaking point, then classifies the breaker type with Iribarren number classifier.

Moreover, to simplify the direct method and reduce computational cost, several machine learning methods were explored. The Figure 26 and 27 show the probability of plunging at a region of image using all the methods in this study. It is clearly shown that the direct approach, SVR regression, and Random Forest yields similar results in two images. Among Neural Networks, Support Vector Machine regression, and Random Forest, the most robust and well performed model is the SVR.

There are few ideas that could be explored if given more time. First, a probability distribution was used for  $H_o$  but not for  $T_o$ , and the distribution of  $T_o$  was not found in the literature. If given more time, the more research and study could be done to find this distribution. Second, there were some issues with the image processing. The unsuitable images are manually and automatically discarded. The screening process was available in the cases of an image missing chunks of a region, not having both of TIMEX and VAR images, and glares in an image. However, the cases of not having a distinct evidence of wave breaking, VAR image's shore not being pitch black, and any light beam pattern present in the image were not able to screen automatically. Convolution or filtering methods are needed to detect their patterns in the images. Third, the result visualization could be automated to overlay images for the final output. Lastly, more labeled and imagery data are needed to classify the breaking types better.

## References

- [1] H. N. Southgate, “Wave breaking-a review of techniques for calculating energy losses in breaking waves,” 1988.
- [2] M. R. Gourlay, *Wave Shoaling and Refraction*, pp. 1149–1154. Dordrecht: Springer Netherlands, 2011.
- [3] J. A. Battjes, “Surf similarity,” in *Coastal Engineering 1974*, pp. 466–480, 1975.
- [4] R. G. Dean, “Equilibrium beach profiles: characteristics and applications,” *Journal of coastal research*, pp. 53–84, 1991.
- [5] R. A. Holman, D. M. Lalejini, K. Edwards, and J. Veeramony, “A parametric model for barred equilibrium beach profiles,” *Coastal Engineering*, vol. 90, pp. 85–94, 2014.
- [6] H. Ghorbanidehno, J. Lee, M. Farthing, T. Hesser, P. K. Kitanidis, and E. F. Darve, “Novel data assimilation algorithm for nearshore bathymetry,” *Journal of Atmospheric and Oceanic Technology*, vol. 36, no. 4, pp. 699–715, 2019.
- [7] K. L. Brodie, M. L. Palmsten, T. J. Hesser, P. J. Dickhudt, B. Raubenheimer, H. Ladner, and S. Elgar, “Evaluation of video-based linear depth inversion performance and applications using altimeters and hydrographic surveys in a wide range of environmental conditions,” *Coastal Engineering*, vol. 136, pp. 147–160, 2018.
- [8] R. A. Holman, D. M. Lalejini, and T. Holland, “A parametric model for barred equilibrium beach profiles: Two-dimensional implementation,” *Coastal Engineering*, vol. 117, pp. 166–175, 2016.
- [9] J. L. Irish and T. White, “Coastal engineering applications of high-resolution lidar bathymetry,” *Coastal engineering*, vol. 35, no. 1-2, pp. 47–71, 1998.
- [10] V. Ramnath, V. Feygels, H. Kalluri, and B. Smith, “Czmil (coastal zone mapping and imaging lidar) bathymetric performance in diverse littoral zones,” in *OCEANS 2015-MTS/IEEE Washington*, pp. 1–10, IEEE, 2015.
- [11] R. Dean and R. Dalrymple, *Water Wave Mechanics for Engineers and Scientists*. Englewood Cliffs, N.J.: Prentice-Hall, 1984.

- [12] E. B. Thornton and R. Guza, “Transformation of wave height distribution,” *Journal of Geophysical Research*, 1983.
- [13] H. Robbins and S. Monro, “A stochastic approximation method,” *The annals of mathematical statistics*, pp. 400–407, 1951.
- [14] W.-Y. Loh, “Classification and regression trees,” *Wiley Interdisciplinary Reviews: Data Mining and Knowledge Discovery*, vol. 1, no. 1, pp. 14–23, 2011.
- [15] “Understanding support vector machine regression.” <https://www.mathworks.com/help/stats/understanding-support-vector-machine-regression.html>. Accessed: 2019-07-24.
- [16] K. L. Brodie, A. Albright, P. J. Hartzell, S. Bak, C. O. Collins III, T. Hesser, and P. Dickhudt, “Multi-beam lidar observations of breaking waves,” in *AGU Fall Meeting Abstracts*, 2018.
- [17] “The coastal imaging lab web.” <http://cil-www.coas.oregonstate.edu>. Accessed: 2019-07-20.